Elpasolite-type Superstructures in Inverse Perovskite Nitrides

Authors: Lukas Link[a], Haichen Wang[b], Thomas Hansen[c], Volodymyr Baran[d], Rainer Niewa[a]

a) Institute of Inorganic Chemistry, Pfaffenwaldring 55, University of Stuttgart, 70569 Stuttgart, Germany
b) Research Center Future Energy Materials and Systems, Universitätsstraße 150, Ruhr University Bochum, 44801 Bochum, Germany
c) Institut Laue-Langevin, 71 avenue des Martyrs, 38042 Grenoble, France
d) Heinz Maier-Leibnitz Zentrum (MLZ), Technical University of Munich, 85748 Garching, Germany

Corresponding author: Rainer Niewa, rainer.niewa@iac.uni-stuttgart.de

Abstract

We present a range of inverse perovskite nitrides with an elpasolite-type superstructure. $(Ca_3N_{0.682(9)})Sn$ and $(Ca_3N_{0.559(7)})Pb$ are variants of the previously described $(Ca_3N)Sn$ and $(Ca_3N)Pb$ which contain less nitrogen and crystallize in $Fm\bar{3}m$. $(Ba_3N_{0.5})Sn$ and $(Ba_3N_{0.5})Pb$ resemble the previously reported perovskites $(Ba_3N_x)Sn$ and $(Ba_3N_x)Pb$, but with both the superstructure and octahedral tilting, resulting in space group $R\bar{3}$. $(Ca_3N_{0.77(2)})Si$, $(Ca_3N_{0.669(6)})Ge$, $(Sr_3N_{0.5})Ge$ and $(Ba_3N_{0.5})Ge$ all crystallize in $P2_1/n$. Among these, only $(Ca_3N_x)Ge$ has been previously described as $(Ca_3N)Ge$. $(Ca_3N_{0.77(2)})Si$ is notably the first compound in which mutually isolated N^{3-} and Si^{4-} ions coexist. There also exists a version with composition $(Ca_3N_{0.86(6)})Si$, which crystallizes in the cubic perovskite aristotype structure with space group $Pm\bar{3}m$. Similarly, there are versions of $(Sr_3N_{0.5})Ge$, $(Ba_3N_{0.5})Sn$ and $(Ba_3N_{0.5})Pb$ with elevated nitrogen contents, less strongly tilted octahedra and no apparent superstructure.

1. Introduction

Perovskites constitute one of the largest and most important families of crystal structures, exhibiting many interesting and useful physical properties such as photoluminescence, superconductivity, giant magnetoresistance and many others. As a consequence, regular perovskites, especially oxides, have been studied extensively. Inverse perovskites (or antiperovskites) have received comparatively less attention. In a regular perovskite with composition $A(BX_3)$, A and B are cations, while X is an anion. In inverse perovskites $(M_3Z)E$, this situation is reversed, such that M represents a cation located on the original X site, while the anions Z and E occupy the B and A sites, respectively. Closely related is the family of metal-rich perovskites, such as $(Ni_3C)Mg$ and Fe_4N, where the only nonmetal atom is located at the B site [1, 2]. True inverse perovskites typically feature metal atoms as cations M, small anions Z from the second period of the periodic table and heavier main group elements as large anions E. Typical representatives of this family of compounds include the oxides of the general composition $(M_3O)Tt$ with M = Ca, Sr, Ba and Tt = Sn, Pb [3], later extended to include Tt = Si, Ge [4, 5, 6]. The discovery of analogous nitrides $(Ca_3N)E$ (E = P, As, Sb, Bi, Ge, Sn, Pb) established nitride as a Z anion [7]. Further advances in this area were made with the discovery of inverse perovskite nitrides of magnesium, strontium and barium [8, 9, 10], as well as the discovery of $(Ca_3N)Tl$ [11]. In the case of the strontium and barium tetrelide compounds, the Z site was found to be only partially occupied by nitrogen [9], which was later confirmed with the discovery of an elpasolite-type superstructure (see figure 1) in the compounds $(Sr_3N_{0.66(7)})Sn$ and $(Sr_3N_{0.68(5)})Pb$ [12].

While powder X-ray diffractometry usually allows for large intensities and therefore excels at the determination of cell parameters and parameters associated with heavy atoms, superstructure reflections of this kind tend to be barely detectable due to the low atomic form factor of nitrogen. In contrast, neutron diffraction is very useful for elucidating such superstructures, as the (coherent) scattering length of nitrogen (9.36 fm) is larger than that of any alkaline earth metal or group 14 element, with the exception of lead (9.41 fm) [13]. X-ray and neutron diffraction patterns can be refined jointly in order to utilize the strengths of both methods.

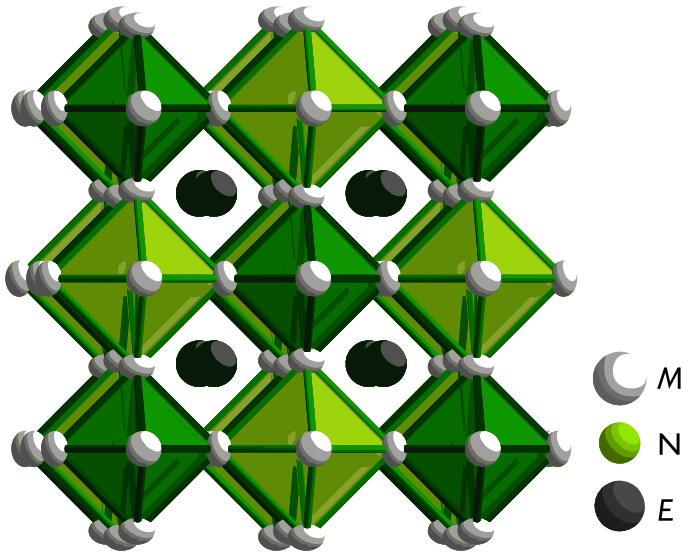

Figure 1: Crystal structure of the $Fm\bar{3}m$ aristotype of the inverse elpasolite nitrides. Dark green octahedra are fully occupied by nitrogen while light green ones may be partially occupied or empty.

Perovskite structures are known for their tendency to distort by octahedral tilting. This tilting may occur along one or more of the three axes of the cubic unit cell and is typically described in terms of Glazer notation [14]. Each tilting scheme leads to a specific reduction in symmetry and is thus linked to a specific space group. Octahedral tilting often induces twinning in perovskite crystals, especially if the twinning occurs when cooling down from an elevated temperature (e.g. the temperature of synthesis).

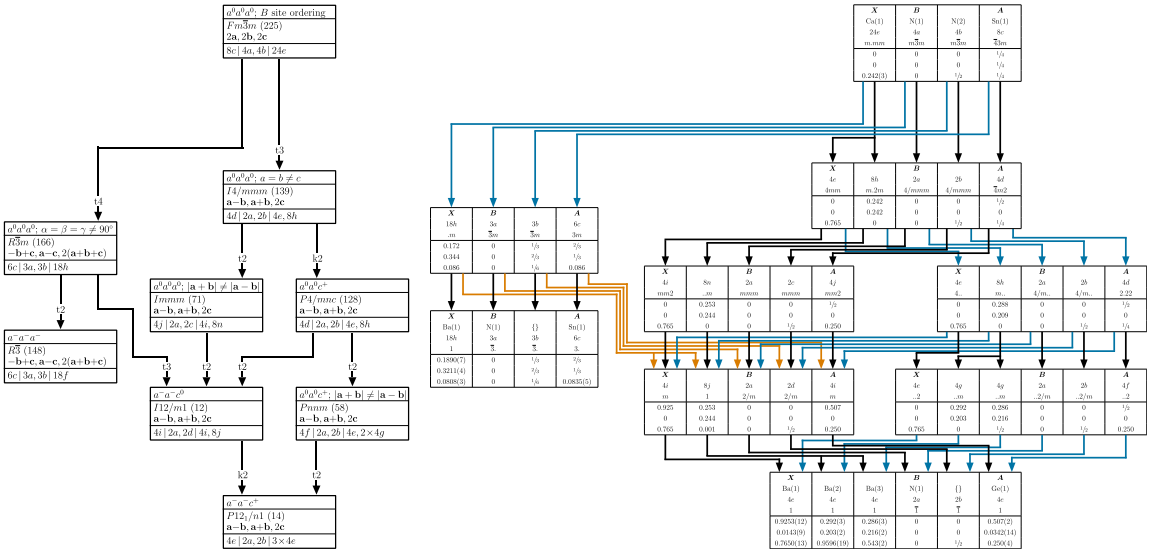

Figure 2: Partial Bärnighausen tree [15] of the tilted elpasolites, showing only the $Fm\overline{3}m$, $R\overline{3}$ and $P2_1/n$ structures discussed in this article, as well as the relevant supergroups. The left hand side of the diagram gives a general overview, while the right hand side depicts the relations of individual crystallographic sites based on examples from among the title compounds where applicable. Unit cells and origin shifts are given in relation to the $Pm\overline{3}m$ perovskite aristotype. See the supporting information for a general overview of the Bärnighausen tree of tilted elpasolites.

One very widely used concept for the characterization of perovskites is the Goldschmidt tolerance factor. This factor predicts with rather high accuracy whether a given perovskite will have tilted octahedra. The underlying model of atoms as hard spheres which touch each other holds very well for regular oxide perovskites. In the case of the title compounds with their 'softer' ions, the Goldschmidt model is not quite as reliable and should be interpreted more as a qualitative trend than as a quantitative instrument [16].

2. Experimental Section

Since many of the reactants and all of the title compounds are sensitive to air, all manipulations were carried out under inert gas. This was facilitated by a glovebox manufactured by M. Braun and operated under argon with at most 1.2 ppm oxygen admitted. The title compounds were synthesized in sodium flux by heating to either 720 °C or 870 °C for several days. The reactions took place in ampoules made from

7 cm long niobium tubes with a diameter of 10 mm and a wall thickness of 0.5 mm. The ampoules were sealed by pinching the ends of the tube, then arc-welding them shut inside the glovebox. In most cases, the respective alkaline earth metals, group 14 elements and sodium amide $NaNH_2$ served as reactants. The hydrogen released by sodium amide is able to diffuse through the niobium walls at the temperature of synthesis. In the cases of $(Sr_3N_{0.5})Ge$ and $(Ba_3N_{0.5})Ge$, sodium amide was replaced as a nitrogen source by germanium nitride Ge_3N_4. After heating, the sodium was removed by extraction with liquid ammonia.

Excess nitrogen tended to lead to the formation of the binary nitrides. Too little nitrogen or too little alkaline earth metal lead to the formation of the M_2E phases (e. g. Sr_2Ge). To prevent this, both were added slightly in excess of the ratios in the target compounds. In the case of the calcium compounds, calcium had to be added in a rather large excess (up to 80 %) to prevent the formation of the Ca_2Tt phases. After heating, this excess was removed along with the sodium. Excessively high temperatures of synthesis also prevented the formation of the target perovskites. While the calcium-based perovskites still formed at 980 °C, this did not hold for the heavier alkaline earth metals. $(Sr_3N_{0.5})Ge$ was synthesized at up to 870 °C, while the barium-based compounds were obtained after heating at 720 °C for three days. Systematic studies on the effect of varying nitrogen contents or temperatures of synthesis were not undertaken.

Several experiments were conducted to expand the range of inverse perovskites to analogous magnesium compounds, as well as the missing silicides $(Sr_3N_x)Si$ and $(Ba_3N_x)Si$. In the former case, products included Mg_3N_2, Mg_2Tt and an unknown soft metal which did not easily dissolve in ammonia. In the case of $(Sr_3N_x)Si$, powder X-ray diffraction data suggest that this compound exists, but it proved difficult to produce a remotely pure sample of it due to the concomitant formation of $SrSiN_2$. $(Ba_3N_x)Si$ was never observed due to the favored formation of $BaSiN_2$.

Samples were analyzed via X-ray and neutron diffraction methods. Neutron diffraction measurements were carried out using the D2B instrument at the Institut Laue-Langevin (ILL) [17], as well as SPODI at the Heinz Meier-Leibniz

Zentrum (MLZ) [18]. Powder samples weighing between 0.7 and 1.5 g were sealed in vanadium cuvettes with the help of single-use indium gaskets. Powder X-ray diffraction measurements were measured in transmission mode on Stoe Stadi-P powder diffractometers using Cu- or Mo-$K_{\alpha 1}$ radiation. To do this, a thin layer of finely ground sample was sealed between two pieces of amorphous foil using vacuum grease. Powder diffraction data were refined via the Rietveld method using Fullprof, with the background fitted by polynomials [19, 20]. Single crystals were measured either on a Bruker-Nonius κ-CCD with Mo-$K_{\alpha 1}$ radiation or on a Stoe StadiVari with Mo- or Ag-$K_{\alpha 1}$ radiation. The obtained data were refined using ShelX 2018 [21].

DFT simulations of the title compounds were computed using VASP [22, 23]. Spin-polarized calculations using the projector augmented wave setups were performed with a cutoff of 520 eV [24, 25]. The Perdew-Burke-Ernzerhof functional was used as exchange-correlation functional [26]. The Brillouin zones were sampled using uniform Γ-centered k-point grids. For geometry optimizations, k-meshes with a density of 800 k-points per reciprocal atom (kppa) were employed. The upper bound for the convergence of forces was set to 0.005 eV/Å. For calculation of total energy, electron localization function (ELF), and density of states (DOS), denser k-grids with 2000 kppa were applied and the total energy was converged below 1 µeV/cell.

For systems with fractional occupation of nitrogen atoms, special quasi-random structures (SQS) were used to simulate a random distribution of occupancies. To generate the SQS, the Alloy Theoretic Automated Toolkit (ATAT) was utilized [27, 28]. To reach the best cell representing the random distribution of nitrogen atoms and defects, the configuration space was searched using a simulated annealing approach [29].

3. Results and Discussion

3.1. Crystal Structures

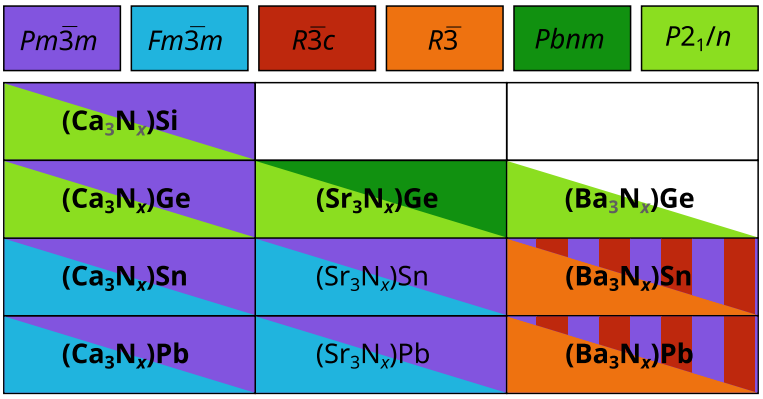

Figure 3: Known structure types of inverse perovskite nitrides $(M_3\mathrm{N}_x)Tt$ with M = Ca, Sr, Ba and Tt = Si, Ge, Sn, Ba. The compounds with rhombohedral, orthorhombic and monoclinic structure types, as well as $(\mathrm{Ca_3N}_x)$Si and the $Fm\bar{3}m$ versions of $(\mathrm{Ca_3N}_x)$Sn and $(\mathrm{Ca_3N}_x)$Pb are first described in this article.

The structures of the title compounds can be derived from the cubic perovskite aristotype. In all cases, an elpasolite-type superstructure is adopted if the nitrogen content is sufficiently low. This is to say the perovskite B site is split into a B and a B' site arranged in a three-dimensional checkerboard pattern. The B site is fully occupied by nitride ions, while the B' site is either empty or partially occupied by nitride ions. In all cases, this leads to a relative *expansion* of the M_6 octahedra centered on the B' site compared to the octahedra centered on and coordinating the atoms on the B site. Figure 3 gives an overview of the inverse perovskite nitrides with and without this superstructure presented in this article, in addition to analogous compounds which have been described previously. Cell parameters are listed in tables 1, 2, 3. Rietveld refinement profiles, data on the single crystal refinements and atom parameters are accessible in the supporting information.

Table 1: Cell parameters for the title compounds with the elpasolite superstructure as determined by joint Rietveld refinement of X-ray and neutron diffraction data, except for $(Ca_3N_{0.77(2)})Si$, where only X-ray diffraction data have been measured. The volume V refers to the pseudocubic perovskite aristotype cell.

compound	space gr.	a / Å	b / Å	c / Å	β / deg	V / Å^3
$(Ca_3N_{0.682(9)})Sn$	$Fm\bar{3}m$	9.83995(5)	a	a	90	119.094(1)
$(Ca_3N_{0.559(7)})Pb$	$Fm\bar{3}m$	9.88709(6)	a	a	90	120.813(1)
$(Ba_3N_{0.5})Sn$	$R\bar{3}$	7.82897(12)	a	19.1111(4)	90	169.073(5)
$(Ba_3N_{0.5})Pb$	$R\bar{3}$	7.84604(12)	a	19.1469(4)	90	170.128(5)
$(Ca_3N_{0.77(2)})Si$	$P2_1/n$	6.8463(9)	6.8399(8)	9.6741(14)	89.913(11)	113.26(3)
$(Ca_3N_{0.669(6)})Ge$	$P2_1/n$	6.8086(5)	6.8328(4)	9.6636(7)	89.990(18)	112.393(13)
$(Sr_3N_{0.5})Ge$	$P2_1/n$	7.27383(8)	7.30982(7)	10.31187(10)	90.012(2)	137.071(2)
$(Ba_3N_{0.5})Ge$	$P2_1/n$	7.6570(4)	7.7300(4)	10.8617(7)	90.062(12)	160.723(18)

Table 2: Cell parameters for the perovskites without a superstructure as determined by Rietveld refinement of X-ray diffraction data, including the volume V of the pseudocubic perovskite aristotype cell.

compound	space gr.	a / Å	b / Å	c / Å	V / Å^3
$(Ba_3N_x)Sn$	$R\bar{3}c$	7.8137(6)	a	19.128(3)	168.57(3)
$(Ba_3N_x)Pb$	$R\bar{3}c$	7.834(5)	a	19.19(2)	170.0(3)
$(Sr_3N_x)Ge$	$Pbnm$	7.2899(7)	7.2880(7)	10.2929(6)	136.71(2)

Table 3: Cell parameters for the title compounds as determined from single crystal X-ray diffraction including the volume V of the pseudocubic perovskite aristotype cell.

compound	space gr.	a / Å	b / Å	c / Å	V / Å^3
$(Ca_3N_{0.86(6)})Si$	$Pm\bar{3}m$	4.8653(5)	a	a	115.17(4)
$(Ca_3N_{0.578(10)})Sn$	$Fm\bar{3}m$	9.8212(9)	a	a	118.413(4)
$(Ca_3N_{0.655(15)})Pb$	$Fm\bar{3}m$	9.8776(2)	a	a	120.466(8)

3.1.1. $(Ca_3N_{0.682(9)})Sn$ and $(Ca_3N_{0.559(7)})Pb$

Given a low enough nitrogen content, $(Ca_3N_{0.682(9)})Sn$ and $(Ca_3N_{0.559(7)})Pb$ directly adopt the inverse $K_2[PtF_6]$ structure type with space group $Fm\bar{3}m$ and the cell parameters given in tables 1 and 3. This is evident from both single crystal and

powder X-ray diffraction, as well as powder neutron diffraction (see the supporting information for more data). In the powder diffraction patterns, the partial ordering of nitrogen atoms and voids is most strongly correlated with the intensity of the 111 reflection. Since nitrogen has a very small atomic form factor due to its low electron count, the 111 reflection barely registers in the X-ray diffraction data (see figure 4). In fact, a significant portion of the intensity of this reflection is only an indirect effect of the ordering, due to the shift of the coordinating calcium atoms towards occupied nitrogen sites. On the other hand, the 111 reflection is much stronger in the neutron diffraction patterns, as can be seen in figure 4. To best make use of the strengths of both methods, X-ray and neutron diffraction patterns were refined jointly using the Rietveld method.

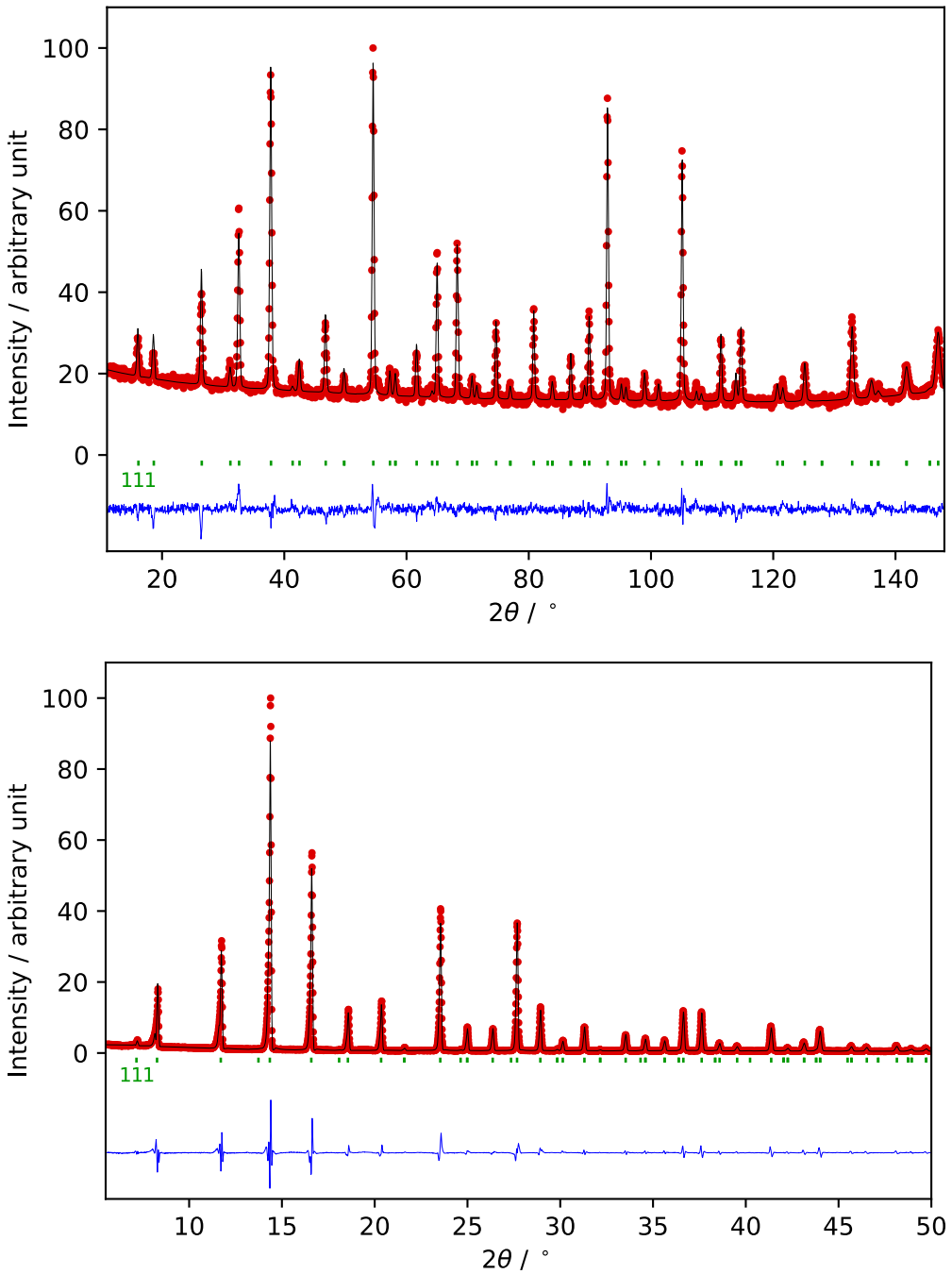

Figure 4: Joint Rietveld refinement profiles (black) of room temperature neutron and X-ray diffraction data for $(Ca_3N_{0.682(9)})Sn$ (red), as well as differences (blue) and Bragg positions (green). Neutron data (top) were collected using neutrons of wavelength 1.5943 Å at the D2B instrument at ILL [17]. X-ray data were collected on a Stoe Stadi-P with Mythen-1K detector using Mo-$K_{\alpha 1}$ radiation.

For $(Ca_3N_{0.682(9)})Sn$ and $(Ca_3N_{0.559(7)})Pb$, neutron diffraction patterns were measured at 10 K in addition to the room temperature data to survey any further symmetry reductions. However, these patterns showed no reflections inconsistent with the $Fm\overline{3}m$ structure model. As expected, the obtained cell parameters were slightly smaller than those measured at room temperature ($a_{(Ca_3N_{0.682(9)})Sn,\ 10\,K} = 9.8075(3)$ Å, $a_{(Ca_3N_{0.559(7)})Pb,\ 10\,K} = 9.87049(18)$ Å, see the supporting material for Rietveld profiles and further information).

3.1.2. $(Ba_3N_{0.5})Sn$ and $(Ba_3N_{0.5})Pb$

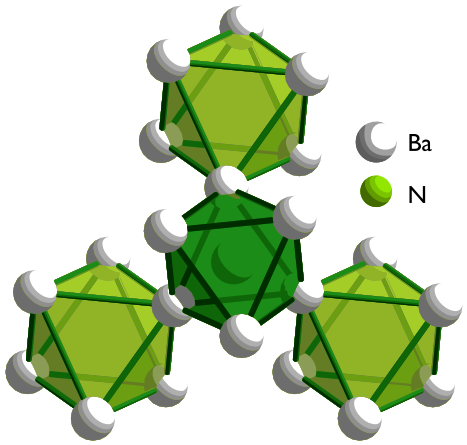

Figure 5: Tilted octahedra in the structure of $(Ba_3N_{0.5})Pb$, viewed along the (hexagonal) **z** axis. The tilting scheme $a^-a^-a^-$ rotates the octahedra around the **z** axis in alternating directions such that the bottom base of the dark green octahedron remains coplanar with the top bases of the light green octahedra. All octahedra retain the symmetry of a trigonal antiprism.

For $(Ba_3N_{0.64(1)})Sn$ and $(Ba_3N_{0.826(4)})Pb$ the perovskite aristotype structure was reported [9]. We were able to reproduce these findings when adding a sufficient amount of nitrogen to the synthesis (at least one quarter of the molar equivalent of barium). The fully ordered compounds $(Ba_3N_{0.5})Sn$ and $(Ba_3N_{0.5})Pb$ were obtained from reactions with nitrogen content close to the ratio in the products. Their elpasolite-type superstructure reflections, while low in intensity, are observable in the X-ray patterns. Their diffraction patterns also feature a number of other low intensity reflections, which arise from octahedral tilting according to Glazer term $a^-a^-a^-$. Together with the superstructure, this reduces the symmetry to space group $R\overline{3}$,

which was confirmed by joint Rietveld refinements of neutron and X-ray diffraction patterns for both compounds.

3.1.3. $(Ca_3N_{0.77(2)})Si$, $(Ca_3N_{0.669(6)})Ge$, $(Sr_3N_{0.5})Ge$ and $(Ba_3N_{0.5})Ge$

$(Ca_3N_{0.77(2)})Si$, $(Ca_3N_{0.669(6)})Ge$, $(Sr_3N_{0.5})Ge$ and $(Ba_3N_{0.5})Ge$ adopt the elpasolite superstructure along with tilted octahedra according to Glazer term $a^-a^-c^+$, which translates to space group $P12_1/n1$. For $(Ca_3N_{0.77(2)})Si$ and $(Ca_3N_{0.669(6)})Ge$, the B' site is partially occupied by nitride ions in a statistical fashion. While $(Ca_3N)Ge$ has been described before with a $Pm\overline{3}m$ perovskite structure and full nitrogen occupancy [7], $(Ca_3N_{0.77(2)})Si$, $(Sr_3N_{0.5})Ge$ and $(Ba_3N_{0.5})Ge$ are presented here for the first time. $(Ca_3N_{0.77(2)})Si$ is notably the first compound which formally contains both Si^{4-} silicide ions and nitride ions.

3.2. Perovskites without the Elpasolite Superstructure

When using slightly more nitrogen than what was necessary to obtain phase pure samples of the elpasolites, in some cases we found perovskites which do not seem to adopt the superstructure and which have not been described before. This includes $(Ba_3N_x)Sn$ and $(Ba_3N_x)Pb$, whose structure contains tilted octahedra according to Glazer term $a^-a^-a^-$, but no apparent superstructure reflections in long exposure X-ray diffraction patterns. This combination corresponds to space group $R\overline{3}c$. However, since neutron diffraction to confirm the absence of nitrogen-defect ordering has not been measured at this time, this space group assignment is still tentative. The same is true for $(Sr_3N_x)Ge$, which adopts a $Pbnm$ structure with tilted octahedra according to $a^-a^-c^+$ when no nitrogen-defect ordering takes place. In all of these cases, we cannot make very precise statements about the nitrogen content, as it is almost without influence on the X-ray diffraction patterns.

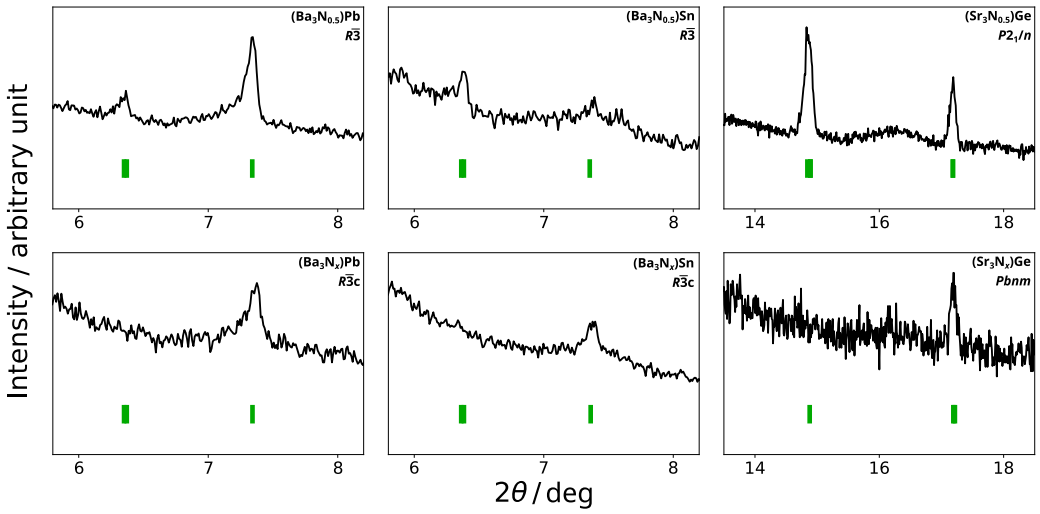

Figure 6: Sections from X-ray diffraction patterns of $(Ba_3N_x)Sn$, $(Ba_3N_x)Pb$ and $(Sr_3N_x)Ge$, with (top) and without (bottom) the elpasolite-type superstructure. Each section contains green lines marking the Bragg position of the strongest superstructure reflection(s) (left) and another reflection of comparable intensity (right). These are the equivalents of the 111 and 002 reflections in the $Fm\bar{3}m$ structure. For the full Rietveld refinement profiles, see the supporting information.

One synthesis attempt yielded a compound with composition $(Ca_3N_{0.86(6)})Si$, which adopts the cubic perovskite aristotype structure according to single crystal X-ray diffraction. When trying to reproduce this compound and the germanium analogon, powder X-ray diffraction patterns often showed broad peaks in place of sharp superstructure reflections, hinting at short-range ordering or possibly the existence of $Fm\bar{3}m$ versions of $(Ca_3N_x)Si$ and $(Ca_3N_x)Ge$ (compare figure 7).

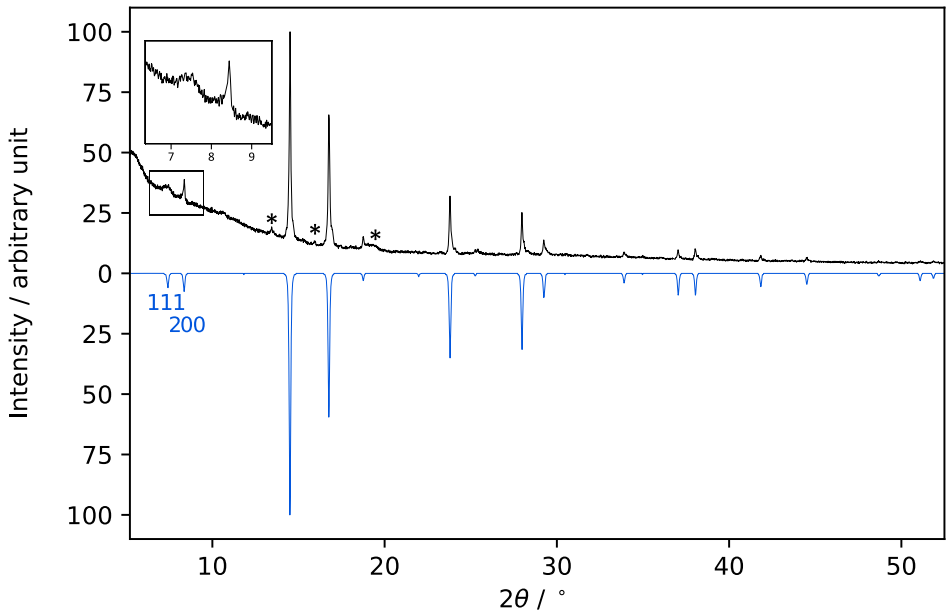

Figure 7: X-ray diffraction pattern of $(Ca_3N_x)Si$ (black) with simulated pattern for the $Fm\bar{3}m$ elpasolite structure (blue). Peaks marked with an asterisk could not be assigned to a reflection, they probably belong to a minor byproduct. The broad reflection in the magnified section corresponds to the strongest superstructure reflection (111) of the $Fm\bar{3}m$ structure, indicating short-range ordering. X-ray data were collected on a Stoe Stadi-P with Mythen-1K detector using Mo-$K_{\alpha 1}$ radiation.

3.3. Geometrical Considerations

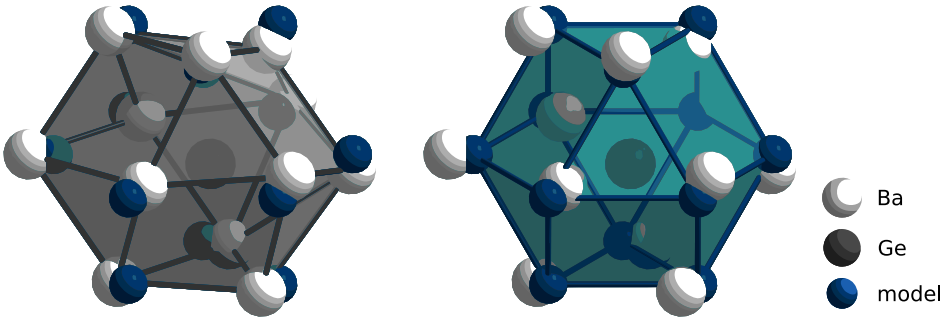

Figure 8: The substantially distorted $GeBa_{12}$ cuboctahedron found in $(Ba_3N_{0.5})Ge$ (grey) compared to the closest fitting model of an Archimedean cuboctahedron (blue).

As illustrated in figure 8, the distortions of the octahedra and cuboctahedra were analyzed by fitting the vertices of appropriate model polyhedra against those of the polyhedra in the crystal structure using Polynator [30]. This program returns

distortion values δ, which are based on the squares of the distances separating these vertex pairs. While the NM_6 octahedra are only slightly distorted ($\delta < 4$), the extent of the distortion from the Archimedean cuboctahedron varies greatly among the TtM_{12} cuboctahedra found in the title compounds (see table 4). It is small in the cubic compounds with space group $Fm\overline{3}m$, where it arises only from the different sizes of the octahedra. In the $R\overline{3}$ compounds, the distortion is still not very large, and the local deviation from the 32 point group is again only caused by the different octahedron sizes. The monoclinic compounds have the most strongly distorted cuboctahedra, which is for the most part due to the tilting of the octahedra. The elpasolite ordering has only a minor effect, as evidenced by the similarity of distortions relative to cuboctahedral models with point groups $m\overline{3}m$ and $\overline{4}3m$. The compounds without the elpasolite superstructure have much less strongly distorted cuboctahedra. This is to some extent due to the lack of the superstructure itself, but for the most part due to their octahedra being less strongly tilted. Overall, there appears to be a clear correlation between the cuboctahedral distortion values and the deviation of the Goldschmidt factor from 1. We can not discern a clear effect of the size difference of the octahedra on the tilting scheme, but octahedra with different sizes seem to exacerbate the extent of the tilting in this limited range of samples.

Table 4: Actual point groups, approximate Goldschmidt tolerance factors f, octahedron sizes as distances d(N–M) and distortion values δ [30] relative to the Archimedean cuboctahedron ($m\bar{3}m$) and a selection of lower symmetry cuboctahedral models. The presented Goldschmidt factors are based on atomic radii compiled in [16] and probably underestimate both the radii of Tt^{4-} anions and the resulting tolerance factor slightly due to limited available data.

compound	point gr. Tt site	f	d_B / Å	$d_{B'}$ / Å	$\delta(m\bar{3}m)$	$\delta(\bar{4}3m)$	$\delta(32)$
$(Ca_3N_{0.682(9)})Sn$	$\bar{4}3m$	0.89	2.376	2.544	2.403	0	2.403
$(Ca_3N_{0.559(7)})Pb$	$\bar{4}3m$	0.89	2.401	2.540	1.980	0	1.980
$(Ba_3N_{0.5})Sn$	3	0.87	2.678	2.869	6.197	5.700	2.431
$(Ba_3N_x)Sn$ ($R\bar{3}c$)	32	0.87	2.765	2.765	3.443	3.443	0
$(Ba_3N_{0.5})Pb$	3	0.87	2.687	2.872	6.223	5.861	2.153
$(Ba_3N_x)Pb$ ($R\bar{3}c$)	32	0.87	2.771	2.771	1.800	1.800	0
$(Ca_3N_{0.77(2)})Si$	1	0.84	2.377	2.502	9.621	9.413	7.800
$(Ca_3N_{0.669(6)})Ge$	1	0.85	2.401	2.445	7.177	7.146	5.820
$(Ba_3N_{0.5})Ge$	1	0.83	2.721	2.852	15.886	15.784	12.035
$(Sr_3N_{0.5})Ge$	1	0.84	2.587	2.671	13.802	13.661	10.403
$(Sr_3N_x)Ge$ ($Pbnm$)	m	0.84	2.598	2.598	9.298	9.298	6.874

3.4. Electronic Structures

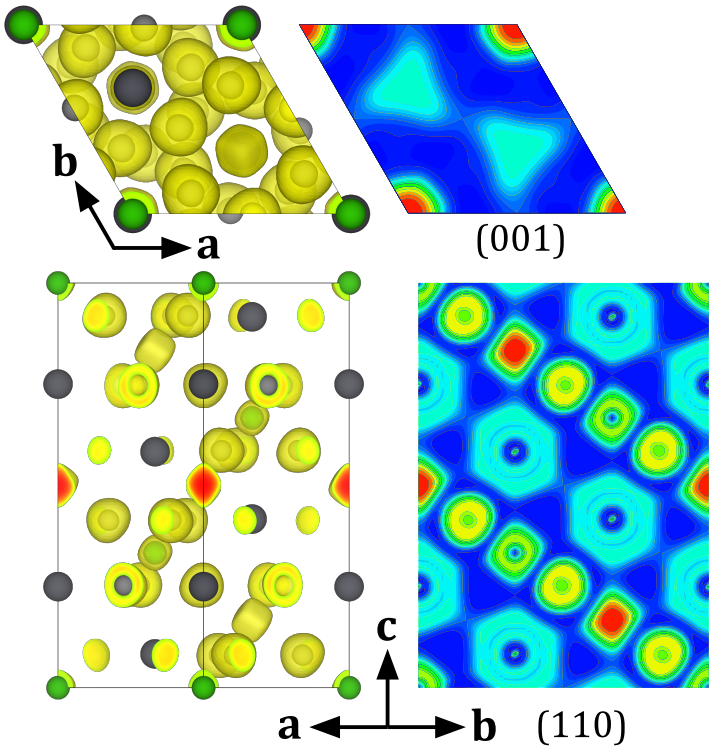

Figure 9: Visualization of the electron localized function (ELF) calculated for $(Ba_3N_{0.5})Pb$. Electron densities displayed here are corrected for the core electrons. When integrated, the actual electron densities in the octahedral voids (red spots) are miniscule, there are fewer than 0.25 electrons in a sphere of radius 1 Å around the empty octahedron center.

Given the electron deficient nature of the $(M_3N_{0.5})Tt$ compounds when understood as (Zintl) ionic compounds, the most obvious explanation is a regular three-dimensional metallic character. However, some other seemingly electron deficient alkaline earth metal nitrides such as the binary compounds Ca_2N, Sr_2N and Ba_2N instead form electrides with electrons confined by certain structural elements [31]. This does not appear to be the case in the title compounds, as, according to the electron localized function (ELF), the electron density is lowest at the center of unoccupied M_6 octahedra and steadily increases when moving closer to the alkaline earth metal atoms. The ELFs are very similar for all title compounds. As figure 9 shows for the example of $(Ba_3N_{0.5})Pb$, there are no covalent bonds or other unusual phenomena.

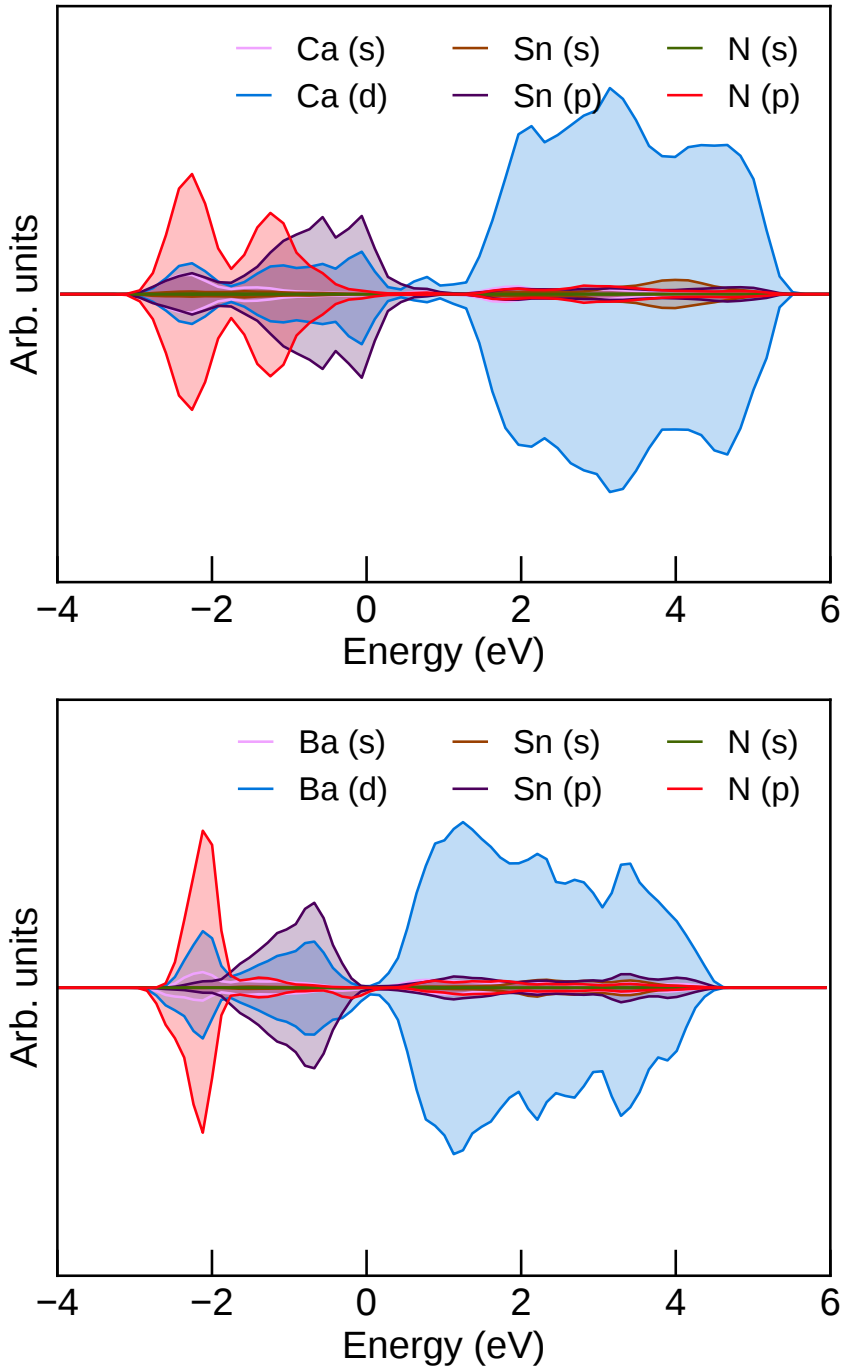

Figure 10: Simulated density of electronic states of $(Ca_3N_{0.65})Sn$ (top, quasirandom structure model) and $(Ba_3N_{0.5})Sn$ (bottom) by atomic orbital type as a function of the energy relative to the Fermi level.

Figure 10 shows diagrams of the computed density of electronic states (DOS) for two of the title compounds (see the supporting information for the rest). In accordance with earlier findings for similar compounds [12], the DOS is non-zero at and immediately above the Fermi level, indicating a metallic nature of the title compounds. In all cases, the band at the Fermi level is dominated by the p electrons of the respective group 14 element and, to a lesser extent, the d electrons of the respective alkaline earth metal elements. At higher energies lies a band fully dominated by the d electrons of the alkaline earth metal elements. This band is separated from the band at the Fermi level by a region with a low, but non-zero density of states. For the strontium and barium compounds, this improper band gap is rather narrow at roughly 0.3 eV and lies directly above the Fermi level. For the calcium compounds, the low density region is slightly wider and located between 0.5 and 1.5 eV above the Fermi level. This suggests that the calcium compounds are significantly better metals, while the strontium and barium compounds are almost semiconductors. It might also help explain why the strontium and barium compounds can be synthesized with 0.5 nitrogen atoms per formula unit with relative ease, while the calcium compounds seem to require a higher nitrogen content, though this is quite speculative.

4. Conclusions

The perovskites of the general formula $(M_3\mathrm{N}_x)Tt$ have a significant homogeneity range when it comes to their nitrogen content. While compositions with $x = \frac{2}{3}$ would satisfy the apparent charge balance of a purely ionic compound, these compounds are shown to have no special preference for such a composition. The lower bound in terms of nitrogen content seems to lie at $x = 0.5$, although we did not succeed in the synthesis of calcium compounds reaching this threshold. Nonetheless, as was shown earlier for $(\mathrm{Sr_3N_{0.59(3)}})\mathrm{Sn}$ and $(\mathrm{Sr_3N_{0.66(7)}})\mathrm{Pb}$ [12], all investigated compounds adopt an elpasolite-type superstructure given a sufficiently low nitrogen content. At $x = 0.5$, the perovskite octahedra are alternately occupied by nitrogen and voids in a three-dimensional checkerboard pattern. This leads to the unoccupied octahedra having a larger size compared to the octahedra occupied by nitrogen. The distribution of the nitrogen atoms on the partially occupied N(2) site of the calcium compounds appears to be statistical. Except for $(\mathrm{Ca_3N_{0.682(9)}})\mathrm{Sn}$ and $(\mathrm{Ca_3N_{0.559(7)}})\mathrm{Pb}$, the title compounds adopt structures with tilted octahedra. Among

these, ($Ba_3N_{0.5}$)Sn and ($Ba_3N_{0.5}$)Pb, which crystallize in $R\overline{3}$, are the least strongly tilted according to the distortion of the cuboctahedra. The tilting in the remaing elpasolite compounds, which all crystallize in $P2_1/n$, is strongest. These findings agree very well with expectations based on the Goldschmidt tolerance factor.

Acknowledgements

We would like to thank Prof. Miguel A. L. Marques for helpful discussions on the SQS methods to simulate structures with statistically occupied sites.

References

[1] P. Höhn, R. Niewa, Nitrides of non-main group elements, Handbook of Solid State Chemistry 1.

[2] R. Niewa, Metal-rich ternary perovskite nitrides, Eur. J. Inorg. Chem. 32 (2019) 3647–3660.

[3] A. Widera, H. Schäfer, Übergangsformen zwischen zintlphasen und echten salzen: Die verbindungen a3bo (mit a = ca, sr, ba und b = sn, pb), Mater. Res. Bull. 15 (1980) 1805–1809.

[4] C. Röhr, Crystal structure of calcium germanide oxide, ca3geo, Z. Kristallogr. 210 (1995) 781.

[5] A. Felden, M. Jansen, Zur kenntnis der inversen perowskite m3to (m = ca, sr, yb; t = si, ge, sn, pb), Z. Anorg. Allg. Chem. 630 (2004) 234–238.

[6] J. Nuss, C. Mühle, K. Hayama, V. Abdolazimi, H. Takagi, Tilting structures in inverse perovskites, m3tto (m = ca, sr, ba, eu; tt = si, ge, sn, pb), Acta Cryst. B 71 (2015) 300–312.

[7] M. Chern, D. Vennos, F. DiSalvo, Synthesis, structure, and properties of anti-perovskite nitrides, J. Solid State Chem. 96 (1992) 415–425.

[8] F. Gäbler, M. Kirchner, W. Schnelle, U. Schwarz, M. Schmitt, H. Rosner, R. Niewa, (sr3n)e and (ba3n)e (e = sb, bi): Synthesis, crystal structures, and physical properties, Z. Anorg. Allg. Chem. 630 (2004) 2292–2298.

[9] F. Gäbler, M. Kirchner, W. Schnelle, M. Schmitt, H. Rosner, R. Niewa, (sr3nx)e and (ba3nx)e (e = sn, pb): Preparation, crystal structures, physical properties and electronic structures, Z. Anorg. Allg. Chem. 631 (2005) 397–402.

[10] E. Chi, W. Kim, N. Hur, D. Jung, New mg-based antiperovskites, Solid State Commun. 121 (2002) 309–312.

[11] R. Niewa, W. Schnelle, F. Wagner, Synthesis, properties and crystal structure of ca3ntl, Z. Anorg. Allg. Chem. 627 (2001) 365–370.

[12] M. Pathak, D. Stoiber, M. Bobnar, A. Ormeci, Y. Prots, R. Niewa, P. Höhn, The inverse perovskite nitrides (sr3n2/3–x)sn, (sr3n2/3–x)pb, and (sr3n)sb: Flux crystal growth, crystal structures, and physical properties, Z. Anorg. Allg. Chem. 644 (2018) 161–167.

[13] V. F. Sears, Neutron scattering lengths and cross sections, Neutron News 3 (1992) 29–37.

[14] A. Glazer, The classification of tilted octahedra in perovskites, Acta Crystallogr. 28 (1972) 3384–3392.

[15] H. Bärnighausen, Group-subgroup relations between space groups, MATCH Commun. Math. Comput. Chem. 9 (1980) 139–175.

[16] R. Niewa, Alkaline-earth metal nitrides of the main-group elements: Crystal structures and properties of inverse perovskites, Z. Anorg. Allg. Chem. 639 (2013) 1699–1715.

[17] A. W. Hewat, D2b - a new high resolution neutron powder diffractormeter at ill grenboble, Mater. Sci. Forum 9 (1986) 69–80.

[18] M. Hoelzel, A. Senyshyn, N. Juenke, H. Boysen, W. Schmahl, H. Fuess, Spodi - high resolution powder diffractometer, Nucl. Instr. A 667 (2012) 32–37.

[19] H. Rietveld, A profile refinement method for nuclear and magnetic structures, J. Appl. Cryst. 2 (1969) 65–71.

[20] J. Rodríguez-Carvajal, Recent advances in magnetic structure determination by neutron powder diffraction, Physica B 192 (1993) 55–69.

[21] G. Sheldrick, A short history of shelx, Acta Crystallogr. A 64 (2008) 112–122.

[22] G. Kresse, J. Furthmüller, Efficiency of ab-initio total energy calculations for metals and semiconductors using a plane-wave basis set, Comput. Mater. Sci. 6 (1996) 15–50.

[23] G. Kresse, J. Furthmüller, Efficient iterative schemes for ab initio total-energy calculations using a plane-wave basis set, Phys. Rev. B 54 (1996) 11169–11186.

[24] P. Blöchl, Projector augmented-wave method, Phys. Rev. B 50 (1994) 17953–17979.

[25] G. Kresse, D. Joubert, From ultrasoft pseudopotentials to the projector augmented-wave method, Phys. Rev. B 59 (1999) 1758–1775.

[26] J. Perdew, K. Burke, M. Ernzerhof, Generalized gradient approximation made simple, Phys. Rev. Lett. 77 (1996) 3865–3868.

[27] A. van de Walle, M. Asta, G. Ceder, The alloy theoretic automated toolkit: A user guide, Calphad 26 (2002) 539–553.

[28] A. van de Walle, Multicomponent multisublattice alloys, nonconfigurational entropy and other additions to the alloy theoretic automated toolkit, Calphad 33 (2009) 266–278.

[29] A. van de Walle, P. Tiwary, M. M. de Jong, D. L. Olmsted, M. D. Asta, A. Dick, D. Shin, Y. Wang, L.-Q. Chen, Z.-K. Liu, Efficient stochastic generation of special quasirandom structures, Calphad 42 (2013) 13–18.

[30] L. Link, R. Niewa, Polynator – a tool to identify and quantitatively evaluate polyhedra and other shapes in crystal structures, J. Appl. Cryst. 56 (2023) in print.

[31] K. Lee, S. Kim, Y. Toda, S. Matsuishi, H. Hosono, Dicalcium nitride as a two-dimensional electride with an anionic electron layer, Nature 494 (2013) 336–340.